Nanoscale Advances

ROYAL SOCIETY OF CHEMISTRY

PAPER

View Article Online
View Journal | View Issue



Cite this: *Nanoscale Adv.*, 2026, **8**, 557

# Low-temperature annealing regulates magneto-acoustic coupling for enhanced FeCoSiB/Ti SAW magnetic field sensor performance

Yutong Wu,[ab] Yining Yin,[a] Baile Cui,[a] Yana Jia,*[a] Hongjie Huang,[c] Hao Wu,[c] Feiming Bai,[c] Wen Wang*[ab] and Xufeng Xue[a]

Utilising low-temperature annealing processes to regulate the magneto-acoustic coupling effect in surface acoustic wave (SAW) magnetic field sensors significantly enhances the sensitivity and temperature stability of sensors. This study employs FeCoSiB/Ti multilayer composite soft magnetic alloys as magneto-sensitive films, combining theoretical modelling with experimental validation to elucidate the multifaceted mechanisms by which low-temperature annealing processes (100 °C) influence the magneto-acoustic coupling effect. Through the Arrhenius magnetic domain reorientation model and the modified Stoney equation, we clarified the use of low-temperature annealing to regulate magnetic parameters such as the saturation magnetostrictive coefficient and internal stress relaxation, thereby enhancing the magnetostrictive thin film $\Delta E$ effect, and ultimately establishing a quantitative relationship between the annealing temperature and the sensitivity of the SAW magnetic sensor. Theoretical analysis demonstrates that after 100 °C annealing, the saturated magnetostrictive coefficient increases to $\lambda_s = 46.9 \times 10^{-6}$, internal stress is significantly reduced, the $\Delta E$ effect improves to 49.5%, and the sensitivity of the SAW magnetic field sensor can be enhanced by 51%. The experimental results verified the theoretical analysis results. After annealing at 100 °C, the sensor sensitivity increased from 156.34° per mT to 236.19° per mT, the temperature drift coefficient decreased by 62.5%, and the insertion loss of the sensor device remained almost unchanged. In contrast, high-temperature annealing at 200 °C/300 °C caused significant lattice distortion and increased acoustic propagation loss, leading to a sharp deterioration in sensitivity (8.67° per mT). This study provides theoretical guidance and experimental evidence for the preparation of SAW magnetic field sensors with high sensitivity and excellent stability.

Received 30th July 2025
Accepted 16th October 2025

DOI: 10.1039/d5na00724k

rsc.li/nanoscale-advances



## 1 Introduction

Surface acoustic wave (SAW) sensor technology is a significant advancement in micro–nano sensing. Its use in magnetic field sensing is facilitating significant cross-disciplinary integration between physics, electronics, and materials science.

SAW magnetic field sensors based on magnetic–acoustic coupling effects have demonstrated marked application potential in precision magnetic field detection fields such as biomedical imaging and inertial navigation due to their wireless passive characteristics,[1] operating in the MHz–GHz frequency range, and excellent electromagnetic interference resistance.[2–4]

Their core magneto-sensitive mechanism originates from the $\Delta E$ effect of magnetostrictive thin films—changes in the material's magnetic state cause alterations in its elastic modulus. Stress transmission at the interface between the piezoelectric substrate and the magneto-sensitive thin film, ultimately results in changes in the SAW propagation velocity ($\Delta v$) and phase ($\Delta \varphi$). This process depends critically on key parameters such as the saturation magnetostrictive coefficient ($\lambda_s$), thin film/substrate interface stress transfer, and acoustic wave mode matching degree.

However, magnetostrictive thin films prepared by magnetron sputtering generally exhibit lattice defects, residual stress, and thermal expansion mismatch issues. These factors adversely affect the sensitivity and temperature stability of sensors.[5] Research shows that local lattice defects (*e.g.*, high concentrations of vacancies) can significantly deteriorate material performance.[6] In addition, non-uniform internal stress in thin films can weaken magnetoelastic coupling efficiency.[7]

Annealing is an effective method for repairing the aforementioned structural defects and optimising magnetic properties. It is widely used to regulate the properties of bulk, thin-strip and thin-film magnetostrictive materials.[8–10] Annealing primarily facilitates internal stress relaxation and reducing defect density, thereby significantly improving magnetic–elastic properties. The annealing effectiveness depends heavily on the material system and temperature. As the annealing temperature

[a]State Key Laboratory of Acoustics, Institute of Acoustics, Chinese Academy of Sciences, Beijing 100190, China. E-mail: wangwenwq@mail.ioa.ac.cn; jiayana@mail.ioa.ac.cn
[b]University of Chinese Academy of Sciences, Beijing 100190, China
[c]School of Electronic Science and Engineering, University of Electronic Science and Technology of China, Chengdu 610054, China

increases, the performance of magneto-sensitive thin films exhibits specific evolutionary patterns. Studies have shown that the $\Delta E$ effect of amorphous TbFeCo thin films deposited on silicon substrates can be enhanced by approximately 30% after annealing.[11] At high annealing temperatures (>500 °C), annealing alters the magnetic domain structure and damping properties of the Fe–16Cr–2.5Mo alloy. Notably, changes in the saturated magnetostrictive coefficient is highly consistent with changes in the damping properties of the annealed samples.[12] Annealing AlN thin films at a medium temperature (600 °C) can slightly optimise the propagation velocity by improving surface morphology of the thin film, but excessive annealing temperatures (*e.g.*, 900 °C) cause the performance deterioration.[9]

Although conventional high-temperature annealing can effectively repair thin-film structures and improve magnetic properties, its application to complete SAW sensor devices containing piezoelectric substrates is problematic. The heat-sensitive piezoelectric substrates are prone to irreversible lattice damage. Additionally, the significant difference in thermal expansion coefficients between the piezoelectric substrate and the thin film can cause severe thermal stress mismatch at high temperatures. Experiments show that annealing temperatures above 250 °C can cause the centre frequency of SAW resonators on ST-cut quartz substrates to drift by hundreds of kHz.[13] Annealing at 400 °C increases the root mean square (RMS) roughness of the surface due to an increase in micro-pores between grains, which in turn causes significant acoustic attenuation when the magnetic field changes,[14] ultimately increasing the insertion loss of the sensor device.[10]

Therefore, controlling the annealing temperature within the low-temperature annealing range is a key strategy for balancing thin-film performance optimisation and substrate thermal damage, thereby effectively improving the magneto-acoustic conversion efficiency. Low-temperature annealing promotes a more uniform, dense structure with fewer defects in piezoelectric,[15] and enhances the bonding strength of the surface $SiO_2$ passivation layer. Experimental observations show that heating samples to 380 K (107 °C) improves the SAW attenuation response by over 1 dB $mm^{-1}$, effectively suppressing the acoustic attenuation caused by high-temperature annealing. Low-temperature vacuum annealing can increase the difference between the maximum and minimum phase shifts by up to 30°.[16] This indicates that low-temperature annealing regulates the interface stress state, thereby providing a more stable propagation path for magneto-acoustic coupling. It is noteworthy that alongside thermal annealing, other strategies such as constructing hybrid composites and employing external energy assistance (*e.g.*, UV illumination) have also been demonstrated as effective pathways to enhance SAW sensor performance.[17] However, the systematic investigation into the multifaceted mechanisms of low-temperature annealing in synergistically regulating magneto-acoustic coupling for SAW magnetic field sensors remains insufficient.

In view of this, this study conducted low-temperature annealing experiments on FeCoSiB/Ti-based SAW magnetic field sensor chips. We systematically investigated the multiple coupling mechanisms involving key parameters (*e.g.*, saturation magnetostriction coefficient, internal stress relaxation, and anisotropy) and established a phenomenological model describing the evolution of the $\Delta E$ effect and magneto-acoustic coupling effect with annealing temperature. This work aims to provide guidance for preparing high-performance SAW magnetic sensors using low-temperature annealing.

## 2 Theoretical model

### 2.1 The $\Delta E$ effect

The $\Delta E$ effect is the core physical mechanism underlying the magnetic sensitivity characteristics of SAW magnetic field sensor devices. Essentially, it refers to the modulation of the elastic modulus caused by changes in the magnetisation state of magnetostrictive thin films under an external magnetic field.

According to the theory of magnetoelastic coupling,[18,19] the expression for magnetoelastic energy density $U_{me}$ is:

$$U_{me} = -\frac{3}{2}\lambda_s \sigma\left(\frac{M^2}{{M_s}^2}\right) \quad (1)$$

where $\lambda_s$ is the saturation magnetostrictive coefficient, $\sigma = \mu_0 MH$ is the magnetostrictive internal stress, $H$ is the external magnetic field strength, and $M$ and $M_s$ are the magnetisation and saturation magnetisation intensity, respectively. The $\Delta E$ effect originates from the change in Young's modulus of magnetostrictive materials under an external magnetic field, and its relative change can be expressed as:

$$\frac{\Delta E}{E} = -\frac{3\sigma\lambda_s}{E_0} \times \frac{1}{1+\frac{K}{\mu_0 {M_s}^2}} \quad (2)$$

$K$ represents the total anisotropy, where $K = K_u + K_\sigma + K_s$, comprising magnetic anisotropy $K_u$, stress anisotropy $K_\sigma$, and structural anisotropy $K_s$. Annealing can regulate the microstructure of FeCoSiB thin films. After annealing, the magnetic domain wall density decreases, leading to an increase in the saturation magnetostrictive coefficient $\lambda_s$. Based on the Arrhenius magnetic domain reorientation model,[20,21] $\lambda_s$ is positively correlated with the annealing temperature:

$$\lambda_s(T) = \lambda_{s0}\left[1 + \alpha \times \exp\left(-\frac{E_a}{k_B T}\right)\right] \quad (3)$$

In the equation, $\alpha$ is the lattice contraction factor. According to the activation energy model in ref. 12, combined with the test data of FeCoSiB/Ti composite thin films obtained by our research group, $\lambda_{s0} = 40 \times 10^{-6}$, $\alpha = 0.15$, $E_a = 0.45$ eV is the magnetic domain activation energy, $k_B$ is the Boltzmann constant, and $T$ is the annealing temperature. Fig. 1(a) illustrates that the annealing temperature is directly proportional to the saturation magnetostriction coefficient. Annealing at 100 °C increases $\lambda_s$ from $40 \times 10^{-6}$ to $46.9 \times 10^{-6}$.

Annealing relaxes the lattice distortion in the magnetostrictive layer, improving the efficiency of stress transfer at the interface and releasing residual thermal stress. The magneto-acoustic coupling effect in SAW magnetic field sensors is the result of the combined action of the multilayer structure. Thermal stress at the film/substrate interface is a key factor causing SAW propagation loss. The Stoney equation can provide

 

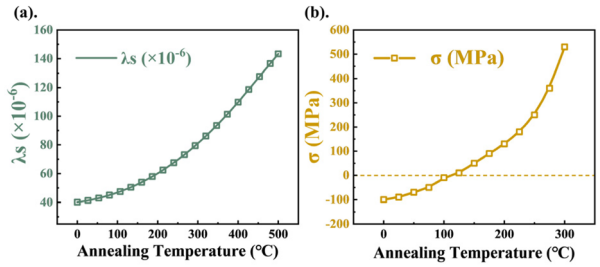


Fig. 1 (a) Saturated magnetostrictive coefficient (b) internal stress *versus* annealing temperature.

the stress under specific conditions.[22,23] Considering the relaxation of thermal stress and intrinsic stress, a stress relaxation model for the thin film is established:

$$\sigma(T) = \left[\sigma_i \times \exp\left(-\frac{T}{T_\sigma}\right)\right] + \left[\frac{E_f}{(1-\nu_f)}\right] \times (\alpha_s - \alpha_f) \times (T - T_{dep}) \quad (4)$$

The first term represents the thermal relaxation of the intrinsic stress in the deposited state, where $\sigma(T)$ is the residual stress in the film after annealing, $\sigma_i$ is the intrinsic stress of the deposited film, and $T_\sigma$ is the characteristic temperature for stress relaxation. The second term is the thermal stress caused by the difference in thermal expansion coefficients between the substrate and the film. $E_f$ and $\nu_f$ are the Young's modulus and Poisson's ratio of the film, $\alpha_s$ and $\alpha_f$ are the thermal expansion coefficients of the substrate and film, and $T_{dep}$ is the deposition temperature. If the yield stress of the material is exceeded, cracking may occur, necessitating annealing to optimise the film deposition. Fig. 1(b) shows the stress evolution of the sample with annealing temperature. In the range from unannealed to annealed at 100 °C, the residual thermal stress manifests as compressive thermal stress. Annealing at 100 °C reduces the interface shear thermal stress from −100 MPa to approximately 0 MPa. Within the 100–200 °C range, the thermal stress remains near zero. However, as the annealing temperature increases further (>200 °C), the thermal stress becomes tensile and increases with temperature. Thus, low-temperature annealing can promote the rearrangement of atoms at the FeCoSiB/Ti multilayer interface and repair microdefects such as lattice distortion and vacancies generated during deposition. Under optimal annealing conditions, the interface becomes denser and uniform. The densified interface can effectively block external temperature disturbances from affecting the magneto sensitive thin film, thereby enhancing the temperature stability of the device alongside sensitivity.

For thin film materials, the easy magnetisation axis is in the [100] direction, and their stress anisotropy field and magnetic anisotropy field are expressed as follows:

$$\begin{cases} H_\sigma = \dfrac{3\lambda_s(T)\sigma(T)}{\mu_0 M_s} \\ H_k = \dfrac{2K_u(T)}{\mu_0 M_s} \end{cases} \quad (5)$$

Magnetic anisotropy $K_u(T)$ decays exponentially with lattice ordering, and stress anisotropy is jointly affected by the saturated magnetostrictive coefficient $\lambda_s$ and internal stress. The stress anisotropy field $H_\sigma$ is an important component of coercivity $H_c$, and its relationship is determined by magnetostriction $\lambda_s$ and internal stress $\sigma$. $H_c$ can be precisely controlled by regulating stress distribution or material composition. The magnetic anisotropy field $H_k$ is determined by crystal symmetry. Structural anisotropy $K_s(T)$ is approximately negligible as defect repair weakens. Therefore, the total anisotropy $K$:

$$K(T) = K_{u0} \exp\left(-\frac{T}{T_k}\right) + \frac{3}{2}\lambda_s(T)\sigma(T) \quad (6)$$

$T_k$ is the magnetic anisotropy characteristic decay temperature, which reflects the rate at which magnetic crystalline anisotropy decays as temperature increases. Therefore, the non-monotonic change in $\Delta E$ with annealing temperature is caused by the competitive evolution of the saturation magnetostrictive coefficient $\lambda_s$, internal stress $\sigma$, and anisotropy $K$. Substituting into eqn (2) yields the complete expression for the $\Delta E$ effect, which includes the Arrhenius magnetic domain reorientation model and the Stoney equation:

$$\frac{\Delta E}{E}(T) = \frac{3}{E_0} \times \left[\sigma_i \times \exp\left(-\frac{T}{T_\sigma}\right) + \beta(T)\right] \times \lambda_{s0}\left(1 + \alpha \times \exp\left(-\frac{E_a}{k_B T}\right)\right) \times \left[1 + \frac{K_u(T) + \frac{3}{2}\lambda_s(T) \times \left[\sigma_i \times \exp\left(-\frac{T}{T_\sigma}\right) + \beta(T)\right]}{\mu_0 {M_s}^2}\right]^{-1} \quad (7)$$

where $\beta(T) = \left[\frac{E_f}{(1-\nu_f)}\right] \times (\alpha_s - \alpha_f) \times (T - T_{dep})$. Fig. 2 shows the variation curve of $\Delta E$ with annealing temperature. Annealing at 100 °C increased the $\Delta E$ effect from 19.58% to 49.5%, while annealing at 200 °C reached the peak value of $\Delta E$. This peak marks the turning point in the competitive relationship between magnetic anisotropy and internal stress relaxation. Low-temperature annealing significantly enhances the $\Delta E$ effect through the synergistic effect of the saturated magnetostrictive coefficient, internal stress, and magnetic anisotropy, thereby

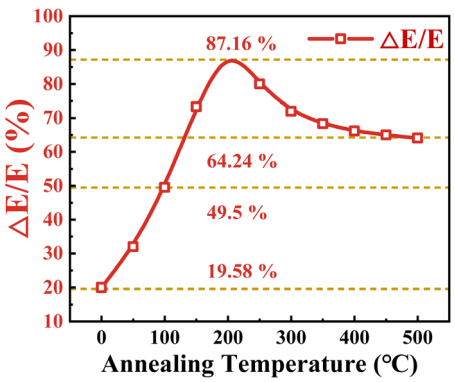


Fig. 2 Relationship between annealing temperature and the $\Delta E$ effect.

improving the magnetic induction characteristics of FeCoSiB/Ti thin films. However, high-temperature annealing further increases the coercivity, which leads to a decrease in the $\Delta E$ effect. In addition, attention should be paid to the possible thermal damage to the substrate at high temperatures and its coupling effect with the thin film. Therefore, factors such as process conditions should be comprehensively considered to determine the optimal annealing temperature.

### 2.2 Magneto-acoustic synergy optimisation

The $\Delta E$ effect modulates the speed and phase of SAW by altering the Young's modulus of the thin film, a process known as the magneto-acoustic coupling effect.[24,25] This section establishes the transfer model for the $\Delta E$-phase sensitivity $S_\psi$. The sensitivity of the SAW sensor ($S = \mathrm{d}\varphi/\mathrm{d}H$) represents the phase response as a function of the external magnetic field and is related to the magneto-acoustic energy conversion efficiency. Its expression can be decomposed as:[26,27]

$$S_\psi = \frac{\mathrm{d}\varphi}{\mathrm{d}H} = \frac{\mathrm{d}\varphi}{\mathrm{d}v} \times \frac{\mathrm{d}v}{\mathrm{d}E} \times \frac{\mathrm{d}E}{\mathrm{d}H} = \frac{\varphi_0}{v_0} \times \frac{\mathrm{d}v}{\mathrm{d}E} \times \frac{\Delta E}{E} \quad (8)$$

where $\frac{\mathrm{d}\varphi}{\mathrm{d}v}$ is the phase of the SAW device as a function of wave velocity, with the following conversion relationship:[28,29]

$$\frac{\Delta v}{v_0} = -\frac{\Delta \varphi}{\varphi_0} \quad (9)$$

$\frac{\mathrm{d}E}{\mathrm{d}H}$ represents the relationship between the change in Young's modulus of the magnetoresistive thin film and the magnetic field strength, *i.e.*, the $\Delta E$ effect. $\frac{\mathrm{d}v}{\mathrm{d}E}$ is the effect of the change in Young's modulus of the propagation substrate on the wave velocity. This study employs a delay-line surface acoustic wave (SAW) magnetic field sensor structure operating at a frequency of 200 MHz. To analyze the intrinsic relationship between the $\Delta E$ effect and phase sensitivity, a finite element simulation model based on resonant and anti-resonant modes of Love waves was established. This model simulates the variation in wave velocity during resonant and anti-resonant states. As shown in Fig. 3(a), building upon the group's prior finite element simulation research,[27] this model systematically describes the evolution of Love wave velocity. This resulted in the simulation curve of the phase change of the SAW magnetic field sensor with annealing temperature shown in Fig. 3(b). As the magnetic field strength increases, the change in $\Delta\varphi$ with annealing temperature follows the same trend as the $\Delta E$ effect. When the external magnetic field reaches 1 mT, the phase change can get about 350° at 100–300 °C. Combined with the stress release situation shown in Fig. 2, the 100–300 °C range has the best stress release effect. At the same time, considering that the quartz has an upper temperature limit, the annealing temperature needs to be adjusted in the actual process to ensure device reliability while improving sensitivity.

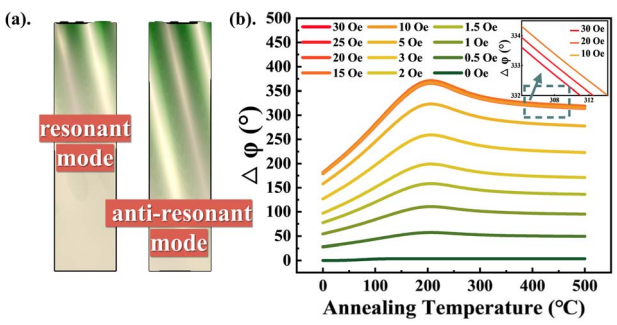


Fig. 3 (a) Finite element simulation model. (b) Simulation curve of the phase variation of SAW magnetic field sensor with annealing temperature.

## 3 SAW sensor fabrication

### 3.1 SAW substrate preparation

In this study, the ST-90°X quartz was utilised as the piezoelectric substrate, and a semiconductor planar process was employed to fabricate a delay-line-type SAW magnetic field sensing substrate with an operating frequency of 200 MHz. The structural diagram is shown in Fig. 4(a). The interdigital transducers (IDTs) consist of aluminium electrodes with a width of 200 nm, with thick fingers measuring 6.24 μm and thin fingers measuring 2.90 μm. Fig. 4(b) presents an optical photograph of the IDT portion of the SAW sensor, captured using a Leica DM8000M optical microscope. The middle layer is a 500 nm-thick $SiO_2$ waveguide layer that acts as an insulating layer. The centre area of the delay line in the top layer constitutes a magnetosensitive thin film coating area. The final stage of the process involved the preparation of a SAW device substrate based on ST-cut 90°X quartz.

### 3.2 Magnetic film preparation and annealing

Magnetically sensitive thin films were deposited on SAW substrates using a direct current (DC) magnetron sputtering method, followed by an annealing process. First, an induced background magnetic field was applied, and the chamber was evacuated to a base pressure of $\leq 8 \times 10^{-3}$ Pa (with a background of 0.3 Pa high-purity argon gas and a radio frequency power of 200 W), followed by sputtering a 10 nm Ti buffer layer. Subsequently, the argon gas pressure was adjusted to 0.5 Pa, and FeCoSiB magnetic film was sputtered at a rate of 10 nm $\mathrm{min}^{-1}$ to a thickness of 100 nm. The process was repeated multiple times until the FeCoSiB thickness reached 300 nm. After film deposition, transfer to a magnetic component vacuum heat treatment device (back vacuum $\leq 8 \times 10^{-3}$ Pa),

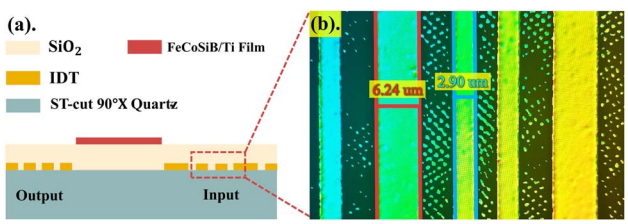


Fig. 4 (a) Schematic diagram of SAW magnetic field sensing chip structure. (b) Magnified image of IDT under the optical microscope.

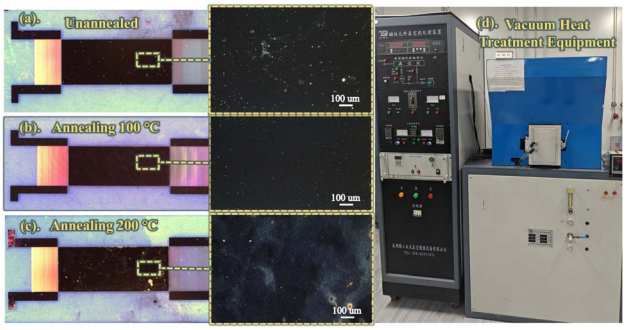


Fig. 5 Actual images of SAW chips and magnetic films (a) unannealed, (b) annealed at 100 °C, (c) annealed at 200 °C, (d) vacuum heat treatment device diagram.

and perform low-temperature annealing for 1 hour under nitrogen protection (heating rate 5 °C $min^{-1}$, furnace cooled to room temperature) to complete low-temperature annealing. Fig. 5(a)–(c) show the physical images of the SAW chip and film, and Fig. 5(d) shows the physical image of the magnetic component vacuum heat treatment device. It was observed that after the 100 °C annealing process, the number of surface defects on the thin film decreased significantly, and the interface became more dense and uniform. Annealing at 200 °C or higher resulted in excessive processing of the thin film surface, leading to further deepening of interface defects. This morphological degradation is directly related to the sharp increase in tensile stress (150 MPa) observed at 200 °C in Fig. 1(b). Although direct XRD characterization was not performed in this study, high-temperature annealing-induced lattice distortion—leading to acoustic wave propagation loss—can be inferred indirectly from the stress model and surface morphology changes (Fig. 5). Subsequent work will incorporate structural characterization methods such as XRD for further validation.

The hysteresis loop and permeability $\mu$–$H$ curve of the thin film were tested using a vibrating sample magnetometer (VSM) and a vector network analyser (VNA, model E5061B). The magnetic film parameters of different annealed FeCoSiB samples (unannealed control group, 100 °C/1 h, 200 °C/1 h, 300 °C/1 h) were measured and summarised in Table 1.

As can be seen from Table 1, the anisotropy field ($H_k$) decreased significantly with the increase in annealing temperature, from 2.205 mT to 1.59 mT; low-temperature annealing (100 °C) reduced the anisotropy field $H_k$ from 2.205 mT to 1.917 mT. The initial permeability ($\mu$) reached its maximum (an increase of 23.62%). This is due to the redistribution of magnetic anisotropy caused by internal stress relaxation, which is consistent with the annealing-induced uniaxial anisotropy reconstruction mechanism observed in ref. 7. Although the $H_k$ value decreased, the simultaneous decrease in coercivity $H_c$ (19% decrease) indicates that the magnetic domain rotation resistance is reduced, which is conducive to enhancing the $\Delta E$ effect. This phenomenon confirms the synergistic optimisation of low anisotropy fields and high permeability in magnetoelastic coupling, rather than simple anisotropy loss. This proves that annealing at 100 °C can effectively eliminate defects introduced during thin film growth and improve film quality. Therefore, the optimal annealing condition was determined to be 100 °C for 1 hour.

Table 1 Parameters of FeCoSiB/Ti magnetic films with different annealing conditions

| Annealing temperature | Unannealed | 100 °C | 200 °C | 300 °C |
|---|---|---|---|---|
| $H_c$ (mT) | 0.211 | 0.171 | 0.194 | 0.201 |
| $H_k$ (mT) | 2.205 | 1.917 | 1.652 | 1.590 |
| Permeability $\mu$ | 982.32 | 1068.69 | 1132.99 | 1214.38 |

## 4 Sensing performance experiments

The experimental setup for characterising the SAW magnetic field sensor consists of a vector network analyser (E5061B), a Helmholtz coil, a direct current (DC) power supply, and a personal computer (PC). The Helmholtz coil generates a stable magnetic field by connecting to an external DC source. The SAW magnetic field sensor is placed in the centre of the coil, and images and experimental data are acquired in real time on the PC.

### 4.1 S21 parameter evaluation

Changes in insertion loss can indirectly indicate the efficiency of acoustic wave propagation. High-temperature annealing (≥200 °C) leads to a significant increase in insertion loss, indicating greater acoustic wave propagation loss. The vector network analyser was used to evaluate the S21 parameters of SAW magnetic field sensor devices at room temperature (24 °C), as shown in Fig. 6. The experimental results show that the insertion loss of the device after annealing at 100 °C is −21.3 dB, which is only 0.87 dB higher than that of the unannealed device (−22.17 dB), and the centre frequency shift is less than 10 kHz. When the annealing temperature was increased to 200 °C, the centre frequency of the device shifted by 50 kHz and the insertion loss increased by 2.78 dB. Annealing at 300 °C caused a centre frequency shift of 70 kHz and an increase in insertion

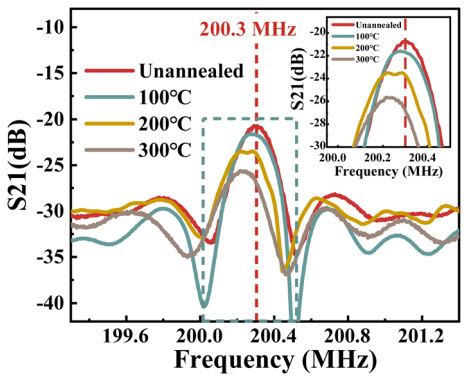


Fig. 6 Effect of annealing on the S21 frequency response curve of SAW magnetic field sensors.

loss of 4.89 dB. When annealing temperatures exceed 300 °C, irreversible lattice damage occurs in the quartz substrate, leading to complete device failure. Consequently, higher temperature experiments were not conducted in this study. Theoretical analysis shows that moderate annealing at 100 °C can improve piezoelectric coupling efficiency by eliminating residual stress, while heat treatment exceeding this temperature threshold may cause quartz substrate lattice distortion, resulting in acoustic surface wave propagation loss, which is consistent with the quartz substrate damage threshold (>250 °C) reported in ref. 13. Therefore, the 100 °C annealing process can effectively optimise the frequency response curve, but exceeding this threshold will cause structural degradation, thereby affecting device performance.

### 4.2 Phase sensitivity experiment

A standard magnetic field of 0–2 mT was applied using a Helmholtz coil, with tests conducted in the 0–0.2 mT range (with 0.02 mT intervals) and the 0.2–2 mT range (with 0.2 mT intervals). A network analyser recorded the phase response changes of the device in real time using a fixed-frequency mode. As shown in Fig. 7, annealing at 100 °C significantly enhances the sensitivity of the SAW magnetic field sensor. When the magnetic field strength is in the range of $0 < H < 0.2$ mT, the phase sensitivity of the 100 °C-annealed device increases from 156.34° per mT to 236.19° per mT compared to the unannealed device, representing a 51% increase; When $H$ increases to 2 mT (where phase changes approach saturation), the maximum response change reaches 266.42°, far exceeding the phase change saturation value of 130.8° for the unannealed device. Annealing at 200 °C has a poor effect on sensitivity improvement (phase sensitivity of 94.93° per mT), but the maximum response value can reach 158.61°, representing a certain improvement compared to the unannealed device; annealing at 300 °C inhibits the sensitivity of the SAW magnetic sensor, with phase sensitivity suddenly dropping to 8.67° per mT.

### 4.3 Temperature stability experiment

The piezoelectric layer of the SAW magnetic field sensor and the thermal expansion effects between layers can cause the device's centre frequency to shift significantly due to changes in ambient temperature. Fig. 8 shows the change in the centre frequency of an unannealed and annealed 100 °C SAW magnetic field sensor with temperature. Tests were conducted at 15 °C intervals within a temperature range of −15 °C to 60 °C. At a low temperature of −15 °C, the centre frequency was 200.325 MHz, and when the operating temperature rose to 60 °C, the centre frequency only decreased slightly to 200.28 MHz. Over the 75 °C temperature range, the entire frequency offset is within 0.045 MHz. This represents a 62.5% reduction compared to the offset (0.12 MHz) of the unannealed device under the same conditions. This demonstrates that low-temperature annealing at 100 °C effectively blocks external temperature disturbances and improves device temperature stability.

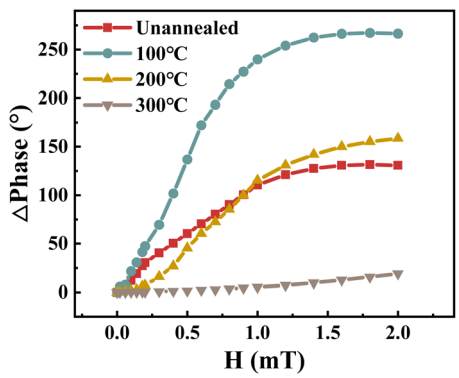


Fig. 7 Phase variation with magnetic field under different annealing conditions.

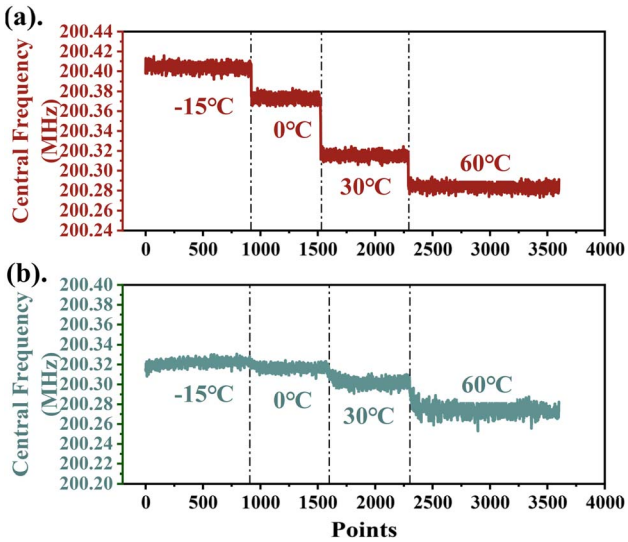


Fig. 8 Comparison of center frequency changes with temperature for (a) unannealed devices and (b) devices annealed at 100 °C.

## 5 Discussion

The superior performance of the SAW magnetic field sensor after 100 °C annealing stems from the synergistic optimization of the FeCoSiB/Ti multilayer film, as demonstrated by the agreement between our theoretical models and experimental results. The enhancement can be attributed to three interconnected physical mechanisms activated by the annealing process.

First, interface stress relaxation plays a critical role. The as-deposited film exhibits a compressive stress of approximately −100 MPa (Fig. 1(b)). Annealing at 100 °C effectively releases this stress, bringing it near zero. This relaxation is directly linked to the 19% reduction in coercivity ($H_c$) (Table 1). A lower $H_c$ indicates that less energy is required for magnetic domain reorientation, as the reduced stress diminishes pinning sites for domain walls. This facilitated magnetization process is essential for efficient magneto-acoustic coupling.

Second, magnetic domain reorientation and the consequent increase in the saturation magnetostrictive coefficient ($\lambda_s$) are

central to the sensitivity enhancement. Our Arrhenius model (eqn (3)) quantitatively predicts the rise in $\lambda_s$ from $40 \times 10^{-6}$ to $46.9 \times 10^{-6}$ at 100 °C (Fig. 1(a)). This predicted enhancement is confirmed by the experimental 51% increase in phase sensitivity (from 156.34° per mT to 236.19° per mT, Fig. 7). Since $\lambda_s$ is a linear factor in the $\Delta E$ effect (eqn (2)), the observed sensitivity gain directly validates the theoretically enhanced $\lambda_s$ and its role in amplifying the $\Delta E$ effect, which is the fundamental mechanism of the sensor.

Third, annealing-induced reduction of magnetic anisotropy works synergistically with the above mechanisms. Data in Table 1 show a clear decrease in the anisotropy field ($H_k$) and a concurrent 23.6% increase in initial permeability ($\mu$) after 100 °C annealing. A lower $H_k$ and higher $\mu$ enable easier rotation of the film's magnetization in response to weak external fields, explaining the improved responsiveness in the low-field region (<0.2 mT) shown in Fig. 7. The competition between this beneficial anisotropy reduction and the performance degradation at higher temperatures (200–300 °C) is captured by our model in Fig. 2, explaining the non-monotonic performance trend.

In synergy, these mechanisms create an optimized magneto-acoustic interface: reduced stress and anisotropy lower the energy barrier for magnetization, while an enhanced $\lambda_s$ maximizes the strain output. This collective action results in a dramatically strengthened $\Delta E$ effect, which jumps from 19.58% to 49.5% (Fig. 2). This robust $\Delta E$ effect is the direct cause of the high sensitivity. Furthermore, the densified and stress-relieved interface, evidenced by the improved surface morphology in Fig. 5(b), provides a more stable acoustic propagation path. This translates directly to the observed 62.5% improvement in temperature stability (Fig. 8), as the device becomes less susceptible to thermo-mechanical perturbations. Thus, the low-temperature annealing strategy successfully engineers the interface physical properties, overcoming the classic trade-off between sensitivity and stability in SAW magnetic sensors.

# 6 Conclusions

This study systematically elucidates the multiple optimization mechanisms of low-temperature annealing (100 °C) on the performance of surface acoustic wave (SAW) magnetic field sensors. Its core innovation lies in the first-ever revelation and verification that low-temperature annealing synergistically enhances both the $\Delta E$ effect and magnetoacoustic coupling efficiency by concurrently regulating the saturated magnetostrictive coefficient, internal stress, and anisotropy of FeCoSiB/Ti multilayer films. Leveraging this magneto-acoustic synergy, the study achieved a 51% increase in sensor sensitivity and a 62.5% improvement in temperature stability without excessive damage to the quartz substrate. This breakthrough effectively overcomes the common technical bottleneck in traditional SAW magnetic field sensors, where sensitivity and temperature stability are difficult to balance simultaneously. This research not only provides new insights and theoretical support for designing high-performance SAW magnetic field sensors but also lays the foundation for their application in high-precision magnetic field measurement.

Subsequent research will focus on optimising the low-temperature annealing process, improving material preparation methods, and sensor structure design to enhance the performance metrics of SAW magnetic field sensors for high-precision magnetic field measurement. Future work will concentrate on further optimising sensor performance, enhancing adaptability in complex environments, and exploring potential applications in other fields.

## Conflicts of interest

There are no conflicts to declare.

## Data availability

All data supporting this study are included in the article.

## Acknowledgements

This work was financially supported by the National Natural Science Foundation of China (no. 12204510 and 12304530), National Key Research and Development Program (2022YFB3206802).

## References

1 F. Muhammad, H. Hong, P. Zhang and Q. Abbas, *Sens. Actuators, A*, 2023, **352**, 114163, DOI: 10.1016/j.sna.2023.114163.
2 P. Mengue, L. Meistersheim, S. Hage-Ali, C. Floer, S. Petit-Watelot, D. Lacour, M. Hehn and O. Elmazria, *IEEE J. Radio Freq. Identif.*, 2023, **7**, 528–535, DOI: 10.1109/JRFID.2023.3299704.
3 H. Zhao, C. Jiao, Q. Wang, C. Gao and J. Sun, *Appl. Sci.*, 2025, **15**(7), 3583, DOI: 10.3390/app15073583.
4 N. Hadjigeorgiou, K. Asimakopoulos, K. Papafotis and P. P. Sotiriadis, *IEEE Sens. J.*, 2021, **21**(11), 12531–12544, DOI: 10.1109/JSEN.2020.3045660.
5 A. Kittmann, P. Durdaut, S. Zabel, J. Reermann, J. Schmalz, B. Spetzler, D. Meyners, N. X. Sun, J. McCord, M. Gerken, *et al.*, *Sci. Rep.*, 2018, **8**(1), 278, DOI: 10.1038/s41598-017-18441-4.
6 K. I. Arai and N. Tsuya, *J. Appl. Phys.*, 1978, **49**(3), 1718–1720, DOI: 10.1063/1.324845.
7 H. Liebermann, C. Graham and P. Flanders, *IEEE Trans. Magn.*, 1977, **13**(5), 1541–1543, DOI: 10.1109/TMAG.1977.1059640.
8 M. Coïsson, G. Barrera, F. Celegato, P. Tiberto and F. Vinai, *J. Phys.: Conf. Ser.*, 2012, **365**, 012003, DOI: 10.1088/1742-6596/365/1/012003.
9 D.-T. Phan and G.-S. Chung, *Appl. Surf. Sci.*, 2011, **257**(20), 8696–8701, DOI: 10.1016/j.apsusc.2011.05.050.
10 D.-T. Phan and G.-S. Chung, *Appl. Surf. Sci.*, 2011, **257**(9), 4339–4343, DOI: 10.1016/j.apsusc.2010.12.053.

11 A. Ludwig and E. Quandt, *IEEE Trans. Magn.*, 2002, **38**(5), 2829–2831, DOI: 10.1109/tmag.2002.802467.
12 Y. Xu and X. Chen, *J. Alloys Compd.*, 2014, **582**, 364–368, DOI: 10.1016/j.jallcom.2013.08.070.
13 R. C. Bray, L. L. Pendergrass, C. A. Johnsen, T. L. Bagwell and J. L. Henderson, in *IEEE 1985 Ultrasonics Symposium*, 1985.
14 Y. Wu, B. Cui, Y. Jia, Z. Zhou, W. Hu, F. Bai, W. Wang, X. Xue and Y. Liang, *Smart Mater. Struct.*, 2024, **33**(5), 055008, DOI: 10.1088/1361-665X/ad37b3.
15 W. Fan, Y. Shuai, X. Pan, W. Luo, C. Wu, S. Huang, L. Wan, Y. Wang and W. Zhang, *Mater. Express*, 2023, **13**(2), 345–351, DOI: 10.1166/mex.2023.2335.
16 O. Marbouh, A. Mazzamurro, O. B. Matar, N. Tiercelin, Y. Dusch, D. Laloy, K. Ettihir, A. Tounzi, A. Benabou and A. Talbi, *IEEE Sens. Lett.*, 2023, **7**(12), 1–4, DOI: 10.1109/LSENS.2023.3330639.
17 K. S. Pasupuleti, A. M. Thomas, D. Vidyasagar, N. Rao, S.-G. Yoon, Y.-H. Kim and S.-G. Kim, *ACS Mater. Lett.*, 2023, **5**(10), 2739–2746.
18 H. Ding, K. Ito, Y. Endo, K. Takanashi and T. Seki, *J. Phys. D: Appl. Phys.*, 2024, **57**(38), 385002, DOI: 10.1088/1361-6463/ad58f0.
19 Y. Qu, Y. Liao, J. He, Y. Chen and G. Yao, *J. Phys. Chem. C*, 2024, **128**(11), 4631–4638, DOI: 10.1021/acs.jpcc.3c06990.
20 W. Tian and C. Hu, *Constr. Build. Mater.*, 2025, **476**, 141298, DOI: 10.1016/j.conbuildmat.2025.141298.
21 Y. Chung and W. H. Green, *Chem. Eng. J.*, 2025, **516**, 163300, DOI: 10.1016/j.cej.2025.163300.
22 H. Nakamura, T. Yamada, T. Igaki, K. Nishimura, T. Ishizaki and K. Ogawa, in *2000 IEEE Ultrasonics Symposium. Proceedings. An International Symposium (Cat. No. 00CH37121)*, IEEE, San Juan, Puerto Rico, 2000, vol. 1.
23 K.-S. Chen and W.-C. Wu, *IEEE Trans. Device Mater. Reliab.*, 2024, **24**(1), 112–122, DOI: 10.1109/TDMR.2024.3352001.
24 W. Hu, M. Huang, H. Zhang and F. Bai, Self-biased SAW magnetic field sensors based on angle dependent magneto-acoustic coupling, *arXiv*, 2022, preprint, DOI: 10.48550/arXiv.2205.14933.
25 W. Hu, M. Huang, Y. Wu, Y. Jia, W. Wang and F. Bai, *Appl. Phys. Lett.*, 2024, **124**(18), 182405, DOI: 10.1063/5.0196523.
26 Y. Sun, W. Wang, Y. Jia, S. Fan and Y. Liang, in *2019 14th Symposium on Piezoelectricity, Acoustic Waves and Device Applications (SPAWDA)*, IEEE, Shijiazhuang, China, 2019.
27 Y. Wu, B. Cui, Y. Sun, Y. Jia, Z. Zhou, W. Hu, F. Bai, X. Xue, Y. Liang and W. Wang, *IEEE Sens. J.*, 2025, **25**(9), 14941–14949, DOI: 10.1109/JSEN.2025.3550896.
28 V. Schell, E. Spetzler, N. Wolff, L. Bumke, L. Kienle, J. McCord, E. Quandt and D. Meyners, *Sci. Rep.*, 2023, **13**(1), 8446, DOI: 10.1038/s41598-023-35525-6.
29 V. Schell, C. Müller, P. Durdaut, A. Kittmann, L. Thormählen, F. Lofink, D. Meyners, M. Höft, J. McCord and E. Quandt, *Appl. Phys. Lett.*, 2020, **116**(7), 073503, DOI: 10.1063/1.5140562.